

# Electronic localization in twisted bilayer MoS<sub>2</sub> with small rotation angle

Somepalli Venkateswarlu,<sup>1</sup> Andreas Honecker,<sup>1</sup> and Guy Trambly de Laissardière<sup>1</sup>

<sup>1</sup>*CY Cergy Paris Université, CNRS, Laboratoire de Physique Théorique et Modélisation (UMR 8089), 95302 Cergy-Pontoise, France*

(Dated: May 26, 2020)

Moiré patterns are known to confine electronic states in transition metal dichalcogenide bilayers, thus generalizing the notion of magic angles discovered in twisted bilayer graphene to semiconductors. Here, we present a revised Slater-Koster tight-binding model that facilitates the first reliable and systematic studies of such states in twisted bilayer MoS<sub>2</sub> for the whole range of rotation angles  $\theta$ . We show that isolated bands appear at low energy for  $\theta \lesssim 5-6^\circ$ . Moreover, these bands become “flatbands”, characterized by a vanishing average velocity, for the smallest angles  $\theta \lesssim 2^\circ$ .

*Introduction.*— Electronic correlations, *i.e.*, the Coulomb interactions between electrons, can give rise to exotic states of matter, with notable examples including Mott insulators [1] and superconductors [2]. Some of the phenomena observed, *e.g.*, in the so-called high-temperature superconductors [3] continue to pose puzzles despite of decades of research. The discovery of electronic localization by a moiré pattern in twisted bilayer graphene [4–7] allows the realization of such phenomena in intrinsically only weakly correlated 2D materials thanks to the emergence of flatbands at low energies that enhances the importance of interactions. Research in this field has been boosted by the experimental discovery of correlated insulators [8] and unconventional superconducting states [9]. In recent years, the broad family of transition metal dichalcogenides (TMDs) [10–12], which offers a wide variety of possible rotationally stacked bilayer systems, has also prompted numerous experimental [13–22] and theoretical [23–37] studies to understand such confined moiré states in semiconductor materials. Many of these studies analyze the interlayer distances, the possible atomic relaxation, the transition from a direct band gap in the monolayer system to an indirect band gap in bilayer systems, and more generally the effect of interlayer coupling in those twisted 2D systems with various rotation angles  $\theta$ . At small values of  $\theta$ , the emergence of flatbands has been established [30] from first-principles density functional theory calculations in twisted bilayer MoS<sub>2</sub> (tb-MoS<sub>2</sub>), and observed in a 3° twisted bilayer WSe<sub>2</sub> sample by using scanning tunneling spectroscopy [22]. Recently, it has been shown numerically [35] that Lithium intercalation in tb-MoS<sub>2</sub> increases interlayer coupling and thus promotes flatbands around the gap. There is also experimental evidence that moiré patterns may give rise to confined states due to the mismatch of the lattice parameters in MoS<sub>2</sub>-WSe<sub>2</sub> heterobilayers [21].

Most theoretical investigations of the electronic structure of bilayer MoS<sub>2</sub> are density-functional theory (DFT) studies [13–18, 23–30, 38–41] with eventually a Wannier wavefunction analysis [24]. Those approaches provide interesting results, but they do not allow a systematic analysis of the electronic structure as a function of the rotation angle  $\theta$ , in particular for small angles, *i.e.*, very large moiré cells, for which DFT calculations are not feasible. Several Tight-Binding (TB) models, based on Slater-Koster (SK) parameters [42], have been proposed for monolayer MoS<sub>2</sub> [43–47] and multi-layer MoS<sub>2</sub> [23, 24, 43, 45]. Following these efforts, we propose

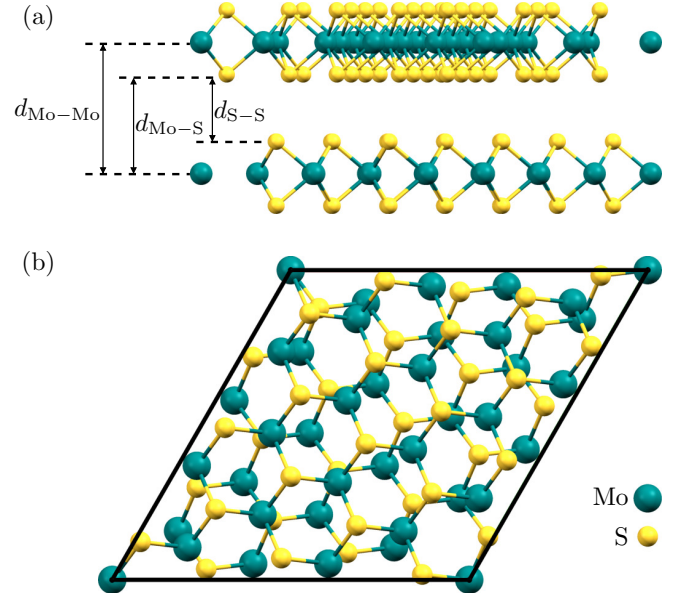


FIG. 1. Atomic structure of bilayer MoS<sub>2</sub> at a twist angle  $\theta = 13.17^\circ$ . (a) side view. (b) top view.

here a Slater-Koster set of parameters that match correctly the DFT bands around the gap of tb-MoS<sub>2</sub> with rotation angles  $\theta > 7^\circ$ . This SK-TB model, with the same parameters, is then used for smaller angles, in order to describe the confined moiré states. We thus show that, for  $\theta \lesssim 6^\circ$ , the valence band with the highest energy is separated from the other valence states by a minigap of a few meV. In addition, the width of this band decreases as  $\theta$  decreases so that the average velocity of these electronic states reaches 0 for  $\theta \lesssim 2^\circ$  such that flatbands emerge at these angles. This is reminiscent of the vanishing of the velocity at certain “magic” rotation angles in bilayer graphene [4–7, 48] except that in the case of bilayer MoS<sub>2</sub> it arises for an interval of angles. Other minigaps and flatbands are also found in the conduction band. The confined states that are closest to the gap are localized in the AA stacking regions of the moiré pattern, like in twisted bilayer graphene.

*Atomic structure.*— The commensurate structure of tb-MoS<sub>2</sub> can be defined in the same manner that is common for twisted bilayer graphene (see for instance Refs. [49, 50]). Here we use the same notation as in Refs. [5, 48]. A commensurate tb-

MoS<sub>2</sub> with rotation angle  $\theta$  is defined by two integers  $n$  and  $m$ , such that

$$\cos \theta = \frac{n^2 + 4nm + m^2}{2(n^2 + nm + m^2)}, \quad (1)$$

and its lattice vectors are  $\vec{r} = n\vec{a}_1 + m\vec{a}_2$  and  $\vec{r}' = -m\vec{a}_1 + (n+m)\vec{a}_2$ , where  $\vec{a}_1$  ( $a\sqrt{3}/2, -a/2, 0$ ) and  $\vec{a}_2$  ( $a\sqrt{3}/2, a/2, 0$ ) are the lattice vectors of monolayer MoS<sub>2</sub>, with the lattice distance  $a = 0.318$  nm. A unit cell of tb-MoS<sub>2</sub> contains  $N = 6(n^2 + nm + m^2)$  atoms. Figure 1 shows a  $(n = 2, m = 3)$  tb-MoS<sub>2</sub> unit cell containing 114 atoms. The cell  $(\vec{a}_1, \vec{a}_2)$  of monolayer MoS<sub>2</sub> contains 3 atoms: Mo at  $(0, 0, 0)$ , S at  $(0, a/\sqrt{3}, 0.49115a)$  and S at  $(0, a/\sqrt{3}, -0.49115a)$  [46, 51]. Note that in tb-MoS<sub>2</sub> different types of moiré cells can be built, as the atoms of a monolayer unit cell are not equivalent by symmetry (see Supplemental Material [52], section I). For simplicity, we consider only moiré patterns constructed as follows in the main text. Starting from an AA stacked bilayer (where Mo atoms of a layer lie above the Mo atoms of the other layer, and S atoms of a layer lie above the S atoms of the other layer), the layer 2 is rotated with respect to the layer 1 by the angle  $\theta$  around a rotation axis going through two Mo atoms. We have checked that the qualitative results presented here are also found in tb-MoS<sub>2</sub> built from an AB stacked bilayer before rotation (see Supplemental Material [52]). The interlayer distance between layers containing Mo atoms is fixed to  $d_{\text{Mo-Mo}} = 0.68$  nm which is the DFT-optimized interlayer distance for AA stacked bilayer MoS<sub>2</sub>. The atomic relaxation probably has an important effect on the electronic structure in tb-MoS<sub>2</sub> [30, 32], like in twisted bilayer graphene [53]. However in this work, our aim is to provide a simple tight-binding (TB) scheme using Slater-Koster parameters that can be used for tb-MoS<sub>2</sub> at all angles in order to analyze qualitatively the electronic states that are confined by the moiré pattern. Indeed, as was the case for twisted bilayer graphene, the study of the non-relaxed structure should make it possible to identify generic properties that will persist with relaxation. Therefore, our numerical results should be qualitatively relevant even if they may not be quantitatively accurate.

*DFT calculations.*— The DFT [54, 55] calculations were carried out with the ABINIT software [56–58] within the Monkhorst-Pack scheme [59] (more details are given in the Supplemental Material [52]). LDA [60] and GGA + Van der Waals [61] exchange-correlation functionals yield very similar results (see Fig. S4 in the Supplemental Material [52]), so all the results presented here are based on LDA calculations, which require less computation time for large systems.

Figure 2 shows DFT bands of tb-MoS<sub>2</sub> along symmetric lines of the first Brillouin zone for four values of the rotation angle  $\theta$ . Note that the size of the Brillouin zones depends on the size of a unit cell of the moiré pattern such that the scale of the horizontal axis varies with  $\theta$ . These bands should be compared with the monolayer bands plotted in the same first Brillouin zone as follows. On the one hand, some bands are not affected by the value of  $\theta$ . Indeed, as shown in Fig. S5 of the Supplemental Material [52], the parabolic band that emanates for the point S<sub>0</sub> is not affected by  $\theta$ . Therefore, we always

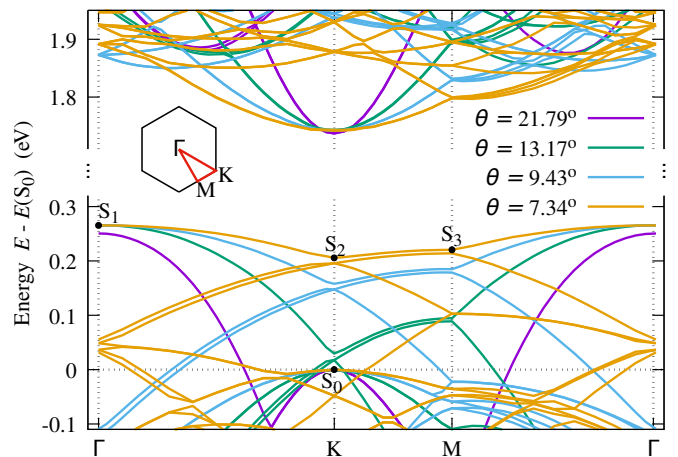


FIG. 2. DFT conduction and valence bands in tb-MoS<sub>2</sub>: (1,2)  $\theta = 21.79^\circ$ , (2,3)  $\theta = 13.17^\circ$ , (3,4)  $\theta = 9.43^\circ$ , and (4,5)  $\theta = 7.34^\circ$ . For every rotation angle, the origin of energy is fixed at the energy of the state S<sub>0</sub>.

set the energy of S<sub>0</sub> to zero. Similarly, for the angles shown in Fig. 2, the curvature of the parabola at the lowest conduction band energy at K is not affected by  $\theta$ . On the other hand, many bands are modified with respect to the monolayer case. Like for simple stacking bilayers (AA, AB, AB', ...) [38–40], the highest valence energy at  $\Gamma$ ,  $E(S_1)$ , increases with respect to the monolayer such that the gap becomes indirect. However,  $E(S_1)$  does not vary significantly with  $\theta$ . In particular for the angles presented in Fig. 2, the curvature of the parabola at S<sub>1</sub> is not affected by  $\theta$  and remains close to that of the monolayer.

Finally, considering the valence band, the most spectacular effect of decreasing  $\theta$  is the increase of the energies of some bands, thus gradually filling the gap. This is, for instance, clearly seen in Fig. 2 when considering the energy variation of the states S<sub>2</sub> and S<sub>3</sub> when  $\theta$  decreases. Similarly, some energies of certain conduction bands decrease as  $\theta$  decreases. Such a  $\theta$  dependence of bands has already been observed for some values of the rotation angle in previous DFT calculations [30]. In order to analyze it systematically, it is necessary to perform calculation for smaller angles which is difficult using DFT calculations. This is the reason why we have developed a TB model that can be used for every value of  $\theta$ .

*TB calculations.*— In a first step, one needs to describe monolayer MoS<sub>2</sub> correctly. The states around the gap at the Fermi energy  $E_F$  are mainly  $4d$  states of Mo [51]. However, to describe valence and conduction bands correctly, it is not sufficient to restrict an effective Hamiltonian to  $4d$  Mo orbitals. Indeed, the ligand field (S atoms) splits the  $4d$  levels of the transition metal (Mo) atoms, and thus creates a direct gap at the K point [51]. Therefore, all TB models proposed in the literature include at least  $3p$  S orbitals [43–47]. Roughly speaking the valence band has mainly  $d_0 = 4d_{z^2}$  Mo character, whereas the conduction band has  $d_0$  character mixed with  $d_2 = 4d_{x^2-y^2}, 4d_{xy}$  Mo character near the gap, and  $d_1 = 4d_{xz}, 4d_{yz}$  Mo character for higher energies [43]. It seems that  $3p$  S orbitals, which have lower on-site energies, act as a

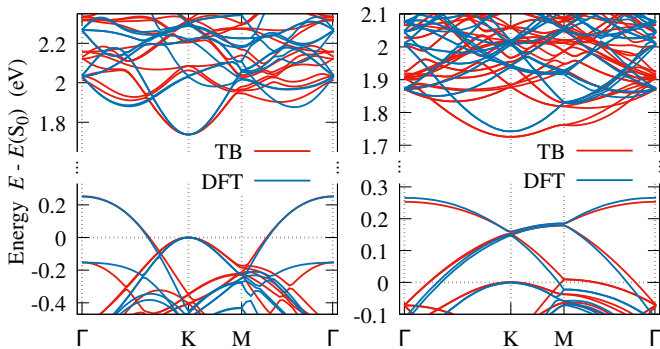


FIG. 3. TB and DFT bands around the gap in tb-MoS<sub>2</sub>: (left) (1,2)  $\theta = 21.79^\circ$  and (right) (3,4)  $\theta = 9.43^\circ$ .

perturbation of the  $4d$  Mo bands. For this reason, several TB models [43, 46, 47] fit rather well to the DFT band structure, while they propose very different parameters (on-site energies and Slater-Koster parameters). Our TB model for monolayer MoS<sub>2</sub> (Fig. S3 in the Supplemental Material [52]) is an adaptation of the model proposed in Ref. [46] for monolayers, and is presented in detail in the Supplemental Material [52]. Each unit cell of the monolayer contains 11 orbitals: 5  $d$  Mo orbitals ( $d_0 = 4d_{z^2}$ ,  $d_1 = 4d_{xz}$ ,  $4d_{yz}$ ,  $d_2 = 4d_{x^2-y^2}$ ,  $4d_{xy}$  of 1 Mo atom) and 6  $p$  S orbitals ( $3p_x$ ,  $3p_y$  and  $3p_z$  of 2 S atoms). Since the precise model may differ for valence and conduction states [46], we have decided to focus on reproducing the valence band accurately. Note that our TB model has been adapted to simulate not only the DFT monolayer bands, but also the DFT bands of twisted bilayers (mainly valence bands), as shown in the following.

In a second step, we consider the coupling between two layers of MoS<sub>2</sub>. Most previous studies [23, 24, 43, 45] include only  $pS - pS$  interlayer coupling terms, but  $dMo - pS$  and  $dMo - dMo$  terms may also be important because we do not limit the interlayer coupling to first-neighbor hopping. Therefore, we include  $pS - pS$ ,  $dMo - pS$ , and  $dMo - dMo$  interlayer terms in our Slater-Koster scheme. It turns out that the latter two are indeed important to reproduce the DFT valence band correctly. An exponential decay with inter-atomic distance [24] and a cutoff function [62] are applied to of these interlayer terms, like in twisted bilayer graphene [48]. Figure 3 shows the comparison between DFT and TB bands for tb-MoS<sub>2</sub> with  $\theta = 21.79^\circ$  and  $9.43^\circ$ . The agreement is excellent for the highest energy valence bands and qualitatively correct for the conduction bands. All parameters of our TB model are given in the Supplemental Material [52].

*Effect of the rotation angle on bands.*— We now analyze the evolution of the bands around the main gap with  $\theta$ . Figure 4 shows this evolution for the top of the valence bands with a focus on the states labeled S<sub>1</sub>, S<sub>2</sub>, S<sub>3</sub>, and S<sub>4</sub>. Both DFT and TB results show that the energies  $E(S_2)$  and  $E(S_3)$  vary almost linearly with  $\theta^2$  (Fig. 4(b)), which is a strong indication that this phenomenon is a direct consequence of the moiré structure. Indeed, in the MoS<sub>2</sub> monolayer, the states around the gap are close to the  $\Gamma$  and K points in reciprocal space,

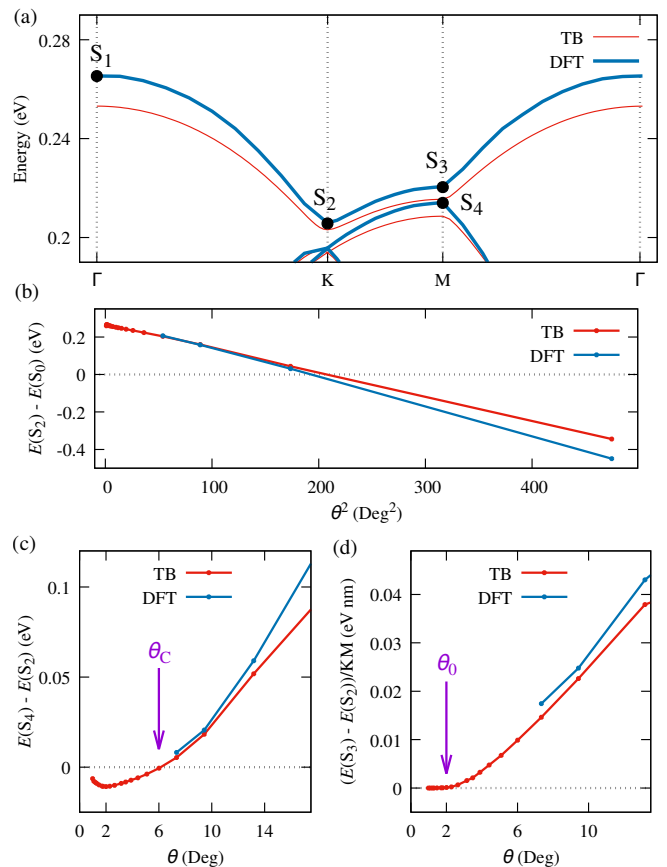


FIG. 4. Dependence of valence bands on rotation angle  $\theta$ : (a) Valence band dispersion of (4,5) tb-MoS<sub>2</sub>,  $\theta = 7.34^\circ$ . (b) Energy  $E(S_2)$  of the state S<sub>2</sub> (see panel (a)) versus  $\theta^2$ . (c) Energy difference between the states S<sub>4</sub> and S<sub>2</sub>,  $\Delta E_{24} = E(S_4) - E(S_2)$ , versus  $\theta$ . A negative value of  $\Delta E_{24}$  means that a gap  $|\Delta E_{24}|$  exists between the band below the gap and the other valence bands. (d) Average slope of  $E(\vec{k})$  of the band between states S<sub>2</sub> and S<sub>3</sub>.

with a parabolic dispersion. In the twisted bilayer, the points  $\Gamma_1$  and  $\Gamma_2$  of the 2 monolayers (layer 1 and layer 2) coincide, while  $K_1$  and  $K_2$  are separated by a small distance  $K_1K_2$  proportional to the angle  $\theta$  for small  $\theta$ . As the monolayer band dispersion is parabolic, the energy of the crossing of the bands of the two layers varies with  $\theta^2$ , and so do the changes in energy induced by the moiré pattern. Similarly, many studies have shown that the changes of energy due to the moiré pattern in twisted graphene bilayer varies linearly with  $\theta$  because the low-energy bands of a graphene monolayer are linear in  $\|\vec{K} - \vec{k}\|$  (see, e.g., Ref. [63]).

Furthermore, our TB computations show that the highest energy valence band is isolated from the remainder of the valence bands by a minigap for sufficiently small values of  $\theta$  (Fig. 5). This is illustrated by Fig. 4(c), showing that  $E(S_4) - E(S_2) < 0$ , *i.e.*, the presence of a minigap, for  $\theta < \theta_c \approx 6^\circ$ . This isolated band is not degenerate, thus it corresponds to one state per moiré cell. Figure 5 shows that such isolated bands are also present among the conduction bands with different values of  $\theta_c$ . Finally, for the smallest angles,

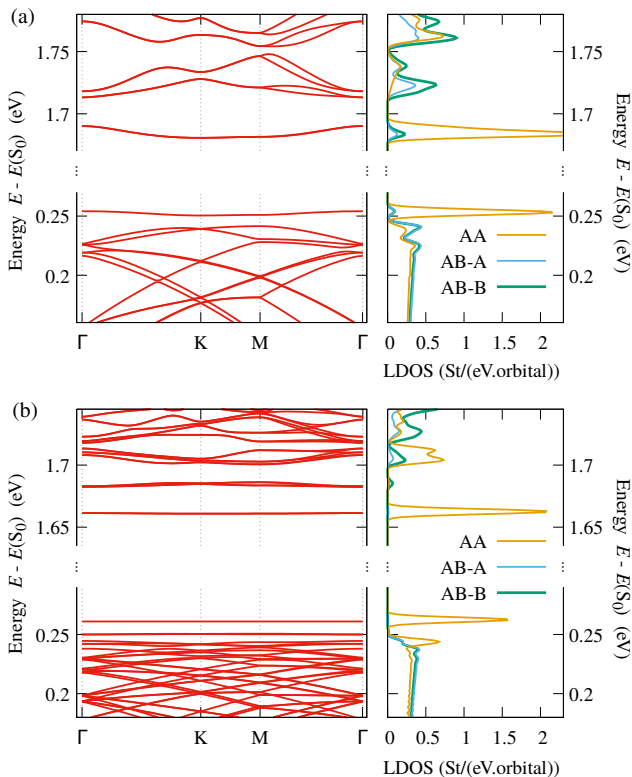


FIG. 5. TB band dispersion and local density of states (LDOS) of  $d_0 = d_2$  Mo atoms at the center of the AA stacking region and the center of the AB region: (a) for (10,11) tb-MoS<sub>2</sub>  $\theta = 3.15^\circ$ , and (b) for (20,21) tb-MoS<sub>2</sub>  $\theta = 1.61^\circ$ . In a moiré cell, two symmetrically equivalent AB stacking regions are located at  $1/3$  and  $2/3$  of the longest diagonal of the cell (see Sec. IA of the Supplemental Material [52]). Each AB stacking region contains two types of Mo atoms: (AB-A) Mo atom of a layer lying above an S atom of the other layer, (AB-B) Mo atom of a layer not lying above an atom of the other layer.

several isolated bands appear both among the valence and conduction bands.

We also consider the average slope of the highest valence band between the points K and M, *i.e.*, between the states  $S_2$  and  $S_3$  (Fig. 4(a)). This quantity is proportional to the average Boltzmann velocity (intra-band velocity). As shown in Fig. 4(d), this velocity tends towards zero for small angles,  $\theta = \theta_0 \approx 2^\circ$ . This demonstrates an electronic confinement corresponding to a “flatband”, like it has been found for twisted bilayer graphene for specific angles, so-called magic angles [4–7, 48]. However, in tb-MoS<sub>2</sub>, this velocity vanishes not only for discrete values of  $\theta$ , but flatbands emerge for a continuous range of  $\theta$ ,  $\theta \leq \theta_0$ .

*Confined state in the AA region of the moiré pattern.*— Like for the monolayer, the electronic states of tb-MoS<sub>2</sub> closest to the gap have mainly  $4d_{z^2}$  Mo character. This is still true for small angles, but states of the isolated bands are mainly localized in the AA stacking region. Consequently, the local density of states (LDOS) for  $4d_{z^2}$  Mo at the center of AA

region contains sharp peaks around the gap (Fig. 5). Note that in the LDOS (Fig. 5), the minigap discussed in the previous paragraph is not seen clearly because of the numerical Gaussian broadening used to calculate the LDOS. Other figures, presented in the Supplemental Material [52], show that the sharp peaks closest to the main gap are found neither in the LDOS of the other  $4d$  Mo orbitals, nor in the LDOS of the Mo atoms that are not located in the AA stacking regions. Thus, the flatband states are confined in AA stacking regions, like in twisted bilayer graphene for small rotation angles [5, 7, 48, 64, 65]. The lowest-energy flatbands (closest to the gap in the valence and conduction bands) are localized at the center of the AA regions, as is also reflected by a strong enhancement of the local density of states in the corresponding regions (Fig. 5), whereas the next flatbands are localized in a ring in the AA regions rather than at their center (see Fig. S9 in the Supplemental Material [52]).

*Conclusion.*— We have revisited the tight-binding description of twisted MoS<sub>2</sub> bilayers starting from DFT computations. Particular attention was paid to interlayer Slater-Koster parameters and we confirmed that not only the closest  $pS - pS$  interlayer coupling terms, but also  $dMo - pS$  and  $dMo - dMo$  coupling needs to be taken into account for an accurate description. We then used this tight-binding model to investigate the band structure of MoS<sub>2</sub> bilayers at smaller rotation angles  $\theta$  where the moiré unit cell becomes too large for DFT computations. We found that isolated bands appear in the valence and conduction bands close to the gap for  $\theta \lesssim 5 - 6^\circ$ . For even smaller angles  $\theta \lesssim 2^\circ$ , the average velocity vanishes. The emergence of the corresponding flatbands is reflected by sharp peaks in the density of states. This phenomenon is accompanied by a localization of the wave function mainly in AA stacking regions. Depending on the flatband, this real-space confinement can occur at the center of AA region and also in a ring around the center of the AA region.

In the present discussion, we have focused on rotated MoS<sub>2</sub> bilayers that are constructed from AA stacking, but we have checked [52] that qualitatively the same behavior is found when one starts from AB stacking instead.

The vanishing velocity and related emergence of flatbands identifies weakly doped MoS<sub>2</sub> bilayers as good candidates for the observation of strong correlation effects. Beyond first theoretical efforts in this direction [36], we offer our DFT-based tight-binding model as a solid starting point for more detailed studies of correlation effects in twisted MoS<sub>2</sub> bilayers.

Note added. Recently, we were alerted of two closely related preprints [66, 67].

*Acknowledgments.*— The authors wish to thank L. Magaud, P. Mallet, D. Mayou, A. Missaoui, J. Vahedi, and J.-Y. Vuillen for fruitful discussions. Calculations have been performed at the Centre de Calculs (CDC), CY Cergy Paris Université and using HPC resources from GENCI-IDRIS (grant A0060910784). We thank Y. Costes and B. Mary, CDC, for computing assistance. This work was supported by the ANR project J2D (ANR-15-CE24-0017) and the Paris//Seine excellence initiative (grant 2017-231-C01-A0).

- [1] N. F. Mott, "The basis of the electron theory of metals, with special reference to the transition metals," *Proc. Phys. Soc. A* **62**, 416–422 (1949).
- [2] J. Bardeen, L. N. Cooper, and J. R. Schrieffer, "Theory of superconductivity," *Phys. Rev.* **108**, 1175–1204 (1957).
- [3] P. A. Lee, N. Nagaosa, and X.-G. Wen, "Doping a Mott insulator: Physics of high-temperature superconductivity," *Rev. Mod. Phys.* **78**, 17–85 (2006).
- [4] J. M. B. Lopes dos Santos, N. M. R. Peres, and A. H. Castro Neto, "Graphene bilayer with a twist: Electronic structure," *Phys. Rev. Lett.* **99**, 256802 (2007).
- [5] G. Trambly de Laissardière, D. Mayou, and L. Magaud, "Localization of Dirac electrons in rotated graphene bilayers," *Nano Letters* **10**, 804–808 (2010).
- [6] E. Suárez Morell, J. D. Correa, P. Vargas, M. Pacheco, and Z. Barticevic, "Flat bands in slightly twisted bilayer graphene: Tight-binding calculations," *Phys. Rev. B* **82**, 121407(R) (2010).
- [7] R. Bistritzer and A. H. MacDonald, "Moiré bands in twisted double-layer graphene," *Proceedings of the National Academy of Sciences* **108**, 12233–12237 (2011).
- [8] Y. Cao, V. Fatemi, A. Demir, S. Fang, S. L. Tomarken, J. Y. Luo, J. D. Sanchez-Yamagishi, K. Watanabe, T. Taniguchi, E. Kaxiras, R. C. Ashoori, and P. Jarillo-Herrero, "Correlated insulator behaviour at half-filling in magic-angle graphene superlattices," *Nature* **556**, 80 (2018).
- [9] Y. Cao, V. Fatemi, S. Fang, K. Watanabe, T. Taniguchi, E. Kaxiras, and P. Jarillo-Herrero, "Unconventional superconductivity in magic-angle graphene superlattices," *Nature* **556**, 43 (2018).
- [10] H. Wang, H. Yuan, S. Sae Hong, Y. Li, and Y. Cui, "Physical and chemical tuning of two-dimensional transition metal dichalcogenides," *Chem. Soc. Rev.* **44**, 2664–2680 (2015).
- [11] G.-B. Liu, D. Xiao, Y. Yao, X. Xu, and W. Yao, "Electronic structures and theoretical modelling of two-dimensional group-VIB transition metal dichalcogenides," *Chem. Soc. Rev.* **44**, 2643–2663 (2015).
- [12] D. L. Duong, S. J. Yun, and Y. H. Lee, "van der Waals layered materials: Opportunities and challenges," *ACS Nano* **11**, 11803–11830 (2017).
- [13] A. M. van der Zande, J. Kunstmann, A. Chernikov, D. A. Chenet, Y. You, X. Zhang, P. Y. Huang, T. C. Berkelbach, L. Wang, F. Zhang, M. S. Hybertsen, D. A. Muller, D. R. Reichman, T. F. Heinz, and J. C. Hone, "Tailoring the electronic structure in bilayer molybdenum disulfide via interlayer twist," *Nano Letters* **14**, 3869–3875 (2014).
- [14] K. Liu, L. Zhang, T. Cao, C. Jin, D. Qiu, Q. Zhou, A. Zettl, P. Yang, S. G. Louie, and F. Wang, "Evolution of interlayer coupling in twisted molybdenum disulfide bilayers," *Nat. Commun.* **5**, 4966 (2014).
- [15] S. Huang, X. Ling, L. Liang, J. Kong, H. Terrones, V. Meunier, and M. S. Dresselhaus, "Probing the interlayer coupling of twisted bilayer MoS<sub>2</sub> using photoluminescence spectroscopy," *Nano Letters* **14**, 5500–5508 (2014).
- [16] S. Huang, L. Liang, X. Ling, A. A. Puretzky, D. B. Geohegan, B. G. Sumpter, J. Kong, V. Meunier, and M. S. Dresselhaus, "Low-frequency interlayer Raman modes to probe interface of twisted bilayer MoS<sub>2</sub>," *Nano Letters* **16**, 1435–1444 (2016).
- [17] C. Zhang, C.-P. Chuu, X. Ren, M.-Y. Li, L.-J. Li, C. Jin, M.-Y. Chou, and C.-K. Shih, "Interlayer couplings, Moiré patterns, and 2D electronic superlattices in MoS<sub>2</sub>/WSe<sub>2</sub> hetero-bilayers," *Science Advances* **3**, e1601459 (2017).
- [18] D. J. Trainer, A. V. Putilov, C. Di Giorgio, T. Saari, B. Wang, M. Wolak, R. U. Chandrasena, C. Lane, T.-R. Chang, H.-T. Jeng, H. Lin, F. Kronast, A. X. Gray, X. Xi, J. Nieminen, A. Bansil, and M. Iavarone, "Inter-layer coupling induced valence band edge shift in mono- to few-layer MoS<sub>2</sub>," *Scientific Reports* **7**, 40559 (2017).
- [19] P.-C. Yeh, W. Jin, N. Zaki, J. Kunstmann, D. Chenet, G. Arefe, J. T. Sadowski, J. I. Dadap, P. Sutter, J. Hone, and R. M. Osgood, Jr., "Direct measurement of the tunable electronic structure of bilayer MoS<sub>2</sub> by interlayer twist," *Nano Letters* **16**, 953–959 (2016).
- [20] M.-L. Lin, Q.-H. Tan, J.-B. Wu, X.-S. Chen, J.-H. Wang, Y.-H. Pan, X. Zhang, X. Cong, J. Zhang, W. Ji, P.-A. Hu, K.-H. Liu, and P.-H. Tan, "Moiré phonons in twisted bilayer MoS<sub>2</sub>," *ACS Nano* **12**, 8770–8780 (2018).
- [21] Y. Pan, S. Fölsch, Y. Nie, D. Waters, Y.-C. Lin, B. Jariwala, K. Zhang, K. Cho, J. A. Robinson, and R. M. Feenstra, "Quantum-confined electronic states arising from the Moiré pattern of MoS<sub>2</sub>-WSe<sub>2</sub> heterobilayers," *Nano Letters* **18**, 1849–1855 (2018).
- [22] Z. Zhang, Y. Wang, K. Watanabe, T. Taniguchi, K. Ueno, E. Tutuc, and B. J. LeRoy, "Flat bands in twisted bilayer transition metal dichalcogenides," *Nature Physics* (2020), 10.1038/s41567-020-0958-x.
- [23] R. Roldán, J. A. Silva-Guillén, M. P. López-Sancho, F. Guinea, E. Cappelluti, and P. Ordejón, "Electronic properties of single-layer and multilayer transition metal dichalcogenides MX<sub>2</sub> (M = Mo, W and X = S, Se)," *Annalen der Physik* **526**, 347–357 (2014).
- [24] S. Fang, R. Kuate Defo, S. N. Shirodkar, S. Lieu, G. A. Tritsarlis, and E. Kaxiras, "Ab initio tight-binding Hamiltonian for transition metal dichalcogenides," *Phys. Rev. B* **92**, 205108 (2015).
- [25] B. Cao and T. Li, "Interlayer electronic coupling in arbitrarily stacked MoS<sub>2</sub> bilayers controlled by interlayer S-S interaction," *The Journal of Physical Chemistry C* **119**, 1247–1252 (2015).
- [26] Z. Wang, Q. Chen, and J. Wang, "Electronic structure of twisted bilayers of graphene/MoS<sub>2</sub> and MoS<sub>2</sub>/MoS<sub>2</sub>," *The Journal of Physical Chemistry C* **119**, 4752–4758 (2015).
- [27] G. C. Constantinescu and N. D. M. Hine, "Energy landscape and band-structure tuning in realistic MoS<sub>2</sub>/MoSe<sub>2</sub> heterostructures," *Phys. Rev. B* **91**, 195416 (2015).
- [28] Y. Tan, F. W. Chen, and A. W. Ghosh, "First principles study and empirical parametrization of twisted bilayer MoS<sub>2</sub> based on band-unfolding," *Applied Physics Letters* **109**, 101601 (2016).
- [29] N. Lu, H. Guo, Z. Zhuo, L. Wang, X. Wu, and X. C. Zeng, "Twisted MX<sub>2</sub>/MoS<sub>2</sub> heterobilayers: effect of van der Waals interaction on the electronic structure," *Nanoscale* **9**, 19131–19138 (2017).
- [30] M. H. Naik and M. Jain, "Ultraflatbands and shear solitons in Moiré patterns of twisted bilayer transition metal dichalcogenides," *Phys. Rev. Lett.* **121**, 266401 (2018).
- [31] F. Conte, D. Ninno, and G. Cantele, "Electronic properties and interlayer coupling of twisted MoS<sub>2</sub>/NbSe<sub>2</sub> heterobilayers," *Phys. Rev. B* **99**, 155429 (2019).
- [32] I. Maity, P. K. Maiti, H. R. Krishnamurthy, and M. Jain, "Reconstruction of moiré lattices in twisted transition metal dichalcogenide bilayers," (2019), arXiv:1912.08702 [cond-mat.mtrl-sci].
- [33] Y. Tang, L. Li, T. Li, Y. Xu, S. Liu, K. Barmak, K. Watanabe, T. Taniguchi, A. H. MacDonald, J. Shan, and K. F. Mak, "Simulation of Hubbard model physics in WSe<sub>2</sub>/WS<sub>2</sub> moiré super-

- lattices,” *Nature* **579**, 353–358 (2020).
- [34] J. Wu, L. Meng, J. Yu, and Y. Li, “A first-principles study of electronic properties of twisted  $\text{MoTe}_2$ ,” *physica status solidi (b)* **257**, 1900412 (2020).
- [35] Z. Lu, S. Carr, D. T. Larson, and E. Kaxiras, “Lithium intercalation in  $\text{MoS}_2$  bilayers and implications for moiré flat bands,” (2020), [arXiv:2004.00238 \[cond-mat.mes-hall\]](https://arxiv.org/abs/2004.00238).
- [36] L. Xian, M. Claassen, D. Kiese, M. M. Scherer, S. Trebst, D. M. Kennes, and A. Rubio, “Realization of nearly dispersionless bands with strong orbital anisotropy from destructive interference in twisted bilayer  $\text{MoS}_2$ ,” (2020), [arXiv:2004.02964 \[cond-mat.mes-hall\]](https://arxiv.org/abs/2004.02964).
- [37] H. Pan, F. Wu, and S. Das Sarma, “Band topology, hubbard model, heisenberg model, and dzyaloshinskii-moriya interaction in twisted bilayer  $\text{wSe}_2$ ,” *Phys. Rev. Research* **2**, 033087 (2020).
- [38] L. Debbichi, O. Eriksson, and S. Lebegue, “Electronic structure of two-dimensional transition metal dichalcogenide bilayers from ab initio theory,” *Phys. Rev. B* **89**, 205311 (2014).
- [39] T. Peng, G. Huai-Hong, Y. Teng, and Z. Zhi-Dong, “Stacking stability of  $\text{MoS}_2$  bilayer: An ab initio study,” *Chinese Physics B* **23**, 106801 (2014).
- [40] J. He, K. Hummer, and C. Franchini, “Stacking effects on the electronic and optical properties of bilayer transition metal dichalcogenides  $\text{MoS}_2$ ,  $\text{MoSe}_2$ ,  $\text{WS}_2$ , and  $\text{WSe}_2$ ,” *Phys. Rev. B* **89**, 075409 (2014).
- [41] F. Sun, T. Luo, L. Li, A. Hong, C. Yuan, and W. Zhang, “Effects of magic angle on crystal and electronic structures of bilayer transition metal dichalcogenides,” (2020), [arXiv:2003.09872 \[cond-mat.mtrl-sci\]](https://arxiv.org/abs/2003.09872).
- [42] J. C. Slater and G. F. Koster, “Simplified LCAO method for the periodic potential problem,” *Phys. Rev.* **94**, 1498–1524 (1954).
- [43] E. Cappelluti, R. Roldán, J. A. Silva-Guillén, P. Ordejón, and F. Guinea, “Tight-binding model and direct-gap/indirect-gap transition in single-layer and multilayer  $\text{MoS}_2$ ,” *Phys. Rev. B* **88**, 075409 (2013).
- [44] H. Rostami, A. G. Moghaddam, and R. Asgari, “Effective lattice Hamiltonian for monolayer  $\text{MoS}_2$ : Tailoring electronic structure with perpendicular electric and magnetic fields,” *Phys. Rev. B* **88**, 085440 (2013).
- [45] F. Zahid, L. Liu, Y. Zhu, J. Wang, and H. Guo, “A generic tight-binding model for monolayer, bilayer and bulk  $\text{MoS}_2$ ,” *AIP Advances* **3**, 052111 (2013).
- [46] E. Ridolfi, D. Le, T. S. Rahman, E. R. Mucciolo, and C. H. Lewenkopf, “A tight-binding model for  $\text{MoS}_2$  monolayers,” *J. Phys.: Condens. Matter* **27**, 365501 (2015).
- [47] J. Á. Silva-Guillén, P. San-Jose, and R. Roldán, “Electronic band structure of transition metal dichalcogenides from ab initio and Slater-Koster tight-binding model,” *Applied Sciences* **6**, 284 (2016).
- [48] G. Trambly de Laissardière, D. Mayou, and L. Magaud, “Numerical studies of confined states in rotated bilayers of graphene,” *Phys. Rev. B* **86**, 125413 (2012).
- [49] J. M. Campanera, G. Savini, I. Suarez-Martinez, and M. I. Heggie, “Density functional calculations on the intricacies of Moiré patterns on graphite,” *Phys. Rev. B* **75**, 235449 (2007).
- [50] E. J. Mele, “Commensuration and interlayer coherence in twisted bilayer graphene,” *Phys. Rev. B* **81**, 161405(R) (2010).
- [51] R. Huisman, R. de Jonge, C. Haas, and F. Jellinek, “Trigonal-prismatic coordination in solid compounds of transition metals,” *Journal of Solid State Chemistry* **3**, 56–66 (1971).
- [52] See Supplemental Material (page 8) the commensurate moiré structures that have been used in the present work, details and complementary results on our DFT calculations, Slater-Koster parameters, and complementary tight-binding results.
- [53] N. N. T. Nam and M. Koshino, “Lattice relaxation and energy band modulation in twisted bilayer graphene,” *Phys. Rev. B* **96**, 075311 (2017).
- [54] P. Hohenberg and W. Kohn, “Inhomogeneous electron gas,” *Phys. Rev.* **136**, B864–B871 (1964).
- [55] W. Kohn and L. J. Sham, “Self-consistent equations including exchange and correlation effects,” *Phys. Rev.* **140**, A1133–A1138 (1965).
- [56] X. Gonze, J.-M. Beuken, R. Caracas, F. Detraux, M. Fuchs, G.-M. Rignanese, L. Sindic, M. Verstraete, G. Zerah, F. Jollet, M. Torrent, A. Roy, M. Mikami, Ph. Ghosez, J.-Y. Raty, and D.C. Allan, “First-principles computation of material properties: the ABINIT software project,” *Computational Materials Science* **25**, 478–492 (2002).
- [57] X. Gonze, B. Amadon, P.-M. Anglade, J.-M. Beuken, F. Bottin, P. Boulanger, F. Bruneval, D. Caliste, R. Caracas, M. Côté, T. Deutsch, L. Genovese, Ph. Ghosez, M. Giantomassi, S. Goedecker, D. R. Hamann, P. Hermet, F. Jollet, G. Jomard, S. Leroux, M. Mancini, S. Mazevet, M. J. T. Oliveira, G. Onida, Y. Pouillon, T. Rangel, G.-M. Rignanese, D. Sangalli, R. Shaltaf, M. Torrent, M. J. Verstraete, G. Zerah, and J. W. Zwanziger, “ABINIT: first-principles approach to material and nanosystem properties,” *Comp. Phys. Commun.* **180**, 2582–2615 (2009).
- [58] X. Gonze, F. Jollet, F. Abreu Araujo, D. Adams, B. Amadon, T. Applencourt, C. Audouze, J.-M. Beuken, J. Bieder, A. Bokhanchuk, E. Bousquet, F. Bruneval, D. Caliste, M. Côté, F. Dahm, F. Da Pieve, M. Delaveau, M. Di Gennaro, B. Dorado, C. Espejo, G. Geneste, L. Genovese, A. Gerossier, M. Giantomassi, Y. Gillet, D. R. Hamann, L. He, G. Jomard, J. Laflamme Janssen, S. Le Roux, A. Levitt, A. Lherbier, F. Liu, I. Lukačević, A. Martin, C. Martins, M. J. T. Oliveira, S. Poncé, Y. Pouillon, T. Rangel, G.-M. Rignanese, A. H. Romero, B. Rousseau, O. Rubel, A. A. Shukri, M. Stankovski, M. Torrent, M. J. Van Setten, B. Van Troeye, M. J. Verstraete, D. Waroquiers, J. Wiktór, B. Xu, A. Zhou, and J. W. Zwanziger, “Recent developments in the ABINIT software package,” *Comp. Phys. Commun.* **205**, 106–131 (2016).
- [59] A. Zupan, P. Blaha, K. Schwarz, and J. P. Perdew, “Pressure-induced phase transitions in solid Si,  $\text{SiO}_2$ , and Fe: Performance of local-spin-density and generalized-gradient-approximation density functionals,” *Phys. Rev. B* **58**, 11266–11272 (1998).
- [60] R. O. Jones and O. Gunnarsson, “The density functional formalism, its applications and prospects,” *Rev. Mod. Phys.* **61**, 689–746 (1989).
- [61] J. P. Perdew, K. Burke, and M. Ernzerhof, “Generalized gradient approximation made simple,” *Phys. Rev. Lett.* **77**, 3865–3868 (1996).
- [62] M. J. Mehl and D. A. Papaconstantopoulos, “Applications of a tight-binding total-energy method for transition and noble metals: Elastic constants, vacancies, and surfaces of monatomic metals,” *Phys. Rev. B* **54**, 4519–4530 (1996).
- [63] I. Brihuega, P. Mallet, H. González-Herrero, G. Trambly de Laissardière, M. M. Ugeda, L. Magaud, J. M. Gómez-Rodríguez, F. Ynduráin, and J.-Y. Veuillen, “Unraveling the intrinsic and robust nature of van Hove singularities in twisted bilayer graphene by scanning tunneling microscopy and theoretical analysis,” *Phys. Rev. Lett.* **109**, 196802 (2012).
- [64] J. M. B. Lopes dos Santos, N. M. R. Peres, and A. H. Castro Neto, “Continuum model of the twisted graphene bilayer,” *Phys. Rev. B* **86**, 155449 (2012).
- [65] O. F. Namarvar, A. Missaoui, L. Magaud, D. Mayou, and

- G. Trambly de Laissardière, “Electronic structure and quantum transport in twisted bilayer graphene with resonant scatterers,” *Phys. Rev. B* **101**, 245407 (2020).
- [66] Z. Zhan, Y. Zhang, G. Yu, F. Guinea, J. Á. Silva-Guillén, and S. Yuan, “Multi-ultraflatbands tunability and effect of spin-orbit coupling in twisted bilayer transition metal dichalcogenides,” (2020), [arXiv:2005.13868 \[cond-mat.mes-hall\]](https://arxiv.org/abs/2005.13868).
- [67] Y. Zhang, Z. Zhan, F. Guinea, J. Á. Silva-Guillén, and S. Yuan, “Tuning band gaps in twisted bilayer MoS<sub>2</sub>,” (2020), [arXiv:2005.13879 \[cond-mat.mes-hall\]](https://arxiv.org/abs/2005.13879).

# Supplemental Material

In this Supplemental Material, we first (section I) present the commensurate moiré structures of twisted bilayer MoS<sub>2</sub> (tb-MoS<sub>2</sub>) that have been used in the present work. Section II gives some details and complementary results on our DFT calculations. Section III provides the Tight-Binding (TB) Slater-Koster parameters for tb-MoS<sub>2</sub>. Complementary TB results (bands, local density of states, and eigenstates) are presented in section IV.

## I. TB-MOS<sub>2</sub> COMMENSURATE STRUCTURES

The atomic structure of commensurate twisted bilayer MoS<sub>2</sub> (tb-MoS<sub>2</sub>) is explained in the main text. The structures of tb-MoS<sub>2</sub> that have been used in the present work are listed table S1.

In tb-MoS<sub>2</sub>, different types of moiré patterns can be built since the atoms of a monolayer unit cell are not equivalent by symmetry. For our study we consider two kinds of moiré patterns:

- **Patterns from AA:** Starting from an AA stacked bilayer (where Mo atoms of a layer lie above a Mo atom of the other layer, and S atoms of a layer lie above an S atom of the other layer), the layer 2 is rotated with respect to layer 1 by the angle  $\theta$  around an axis containing two Mo atoms.
- **Patterns from AB:** Starting from an AB stacked bilayer (where Mo atoms of layer 1 lie above a Mo atom of layer 2, and S atoms of each layer do not lie above an atom of the other layer), layer 2 is rotated with respect to layer 1 by the angle  $\theta$  around an axis containing two Mo atoms.

For simplicity, in the main text we discussed only moiré patterns built from AA stacking, but results for moiré patterns built from AB stacking yield similar results, as shown here.

### A. Moiré pattern from AA

Figure S1 shows a top view of the atomic structure of (6,7) tb-MoS<sub>2</sub> built from AA stacking. One can identify several specific types of stacking regions:

- AA stacking regions are regions where Mo atoms of a layer lie above a Mo atom of the other layer, and S atoms of a layer lie above an S atom of the other layer.
- AB' stacking regions are regions where Mo atoms of layer 1 lie above an S atom of layer 2, and S atoms of layer 1 (Mo atoms of layer 2) do not lie above an atom of layer 2 (layer 1).
- BA' stacking regions are regions where S atoms of layer 1 atoms lie above a Mo atom of layer 2, and Mo atoms

TABLE S1.  $(n,m)$  twisted bilayer MoS<sub>2</sub> (tb-MoS<sub>2</sub>) structures that have been used in the present work.  $\theta$  is the rotation angle between the two layers and  $N$  the number of atoms in a unit cell.

$(n,m)$	$\theta$ [deg.]	$N$
(1,2)	21.787	42
(2,3)	13.174	114
(3,4)	9.430	222
(4,5)	7.341	366
(5,6)	6.009	546
(6,7)	5.086	762
(7,8)	4.408	1014
(10,11)	3.150	1986
(15,16)	2.134	4326
(16,17)	2.004	4902
(18,19)	1.788	6162
(19,20)	1.696	6846
(20,21)	1.614	7566
(22,23)	1.470	9114
(25,26)	1.297	11706
(27,28)	1.203	13614
(30,31)	1.085	16746
(33,34)	0.987	20202
(36,37)	0.906	23982

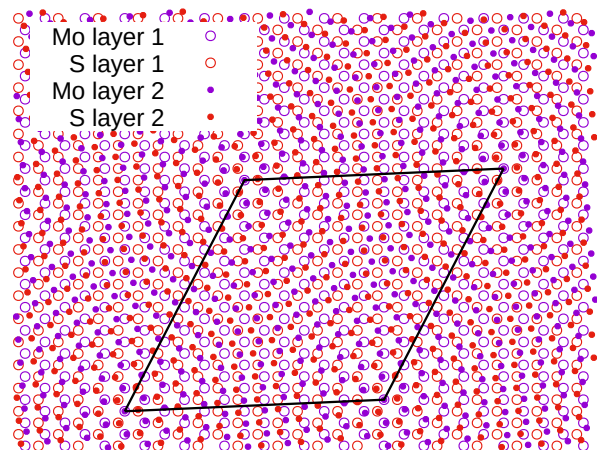


FIG. S1. Atomic structure of (6,7) tb-MoS<sub>2</sub> built from AA stacked bilayers. Black lines show the unit cell. AA stacking regions are at the corners of this cell, BA' and AB' stacking regions are at 1/3 and 2/3 of its longest diagonal, respectively.

of layer 1 (S atoms layer 2) do not lie above an atom of layer 2 (layer 1).

In Fig. S1, AA stacking regions are located at the corners of the moiré cell. BA' and AB' stacking regions are located at



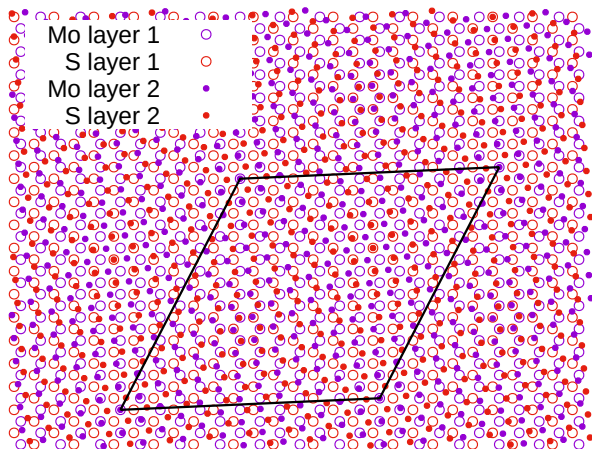


FIG. S2. Atomic structure of (6,7) tb-MoS<sub>2</sub> built from AB stacked bilayers. Black lines show the unit cell. AB stacking regions are at the corners of this cell, AA' and BA stacking regions are at 1/3 and 2/3 of the longest diagonal, respectively.

1/3 and 2/3 of its long diagonal, respectively.

### B. Moiré pattern from AB

Figure S2 shows a top view of the atomic structure of (6,7) tb-MoS<sub>2</sub> built from AB stacking. Here one can identify several specific types of stacking regions:

- AA' stacking regions are regions where Mo atoms (S atoms) of one layer lie above an S atom (Mo atom) of the other layer.
- AB stacking regions are regions where Mo atoms of layer 1 lie above a Mo atom of layer 2, and S atoms of each layer do not lie above an atom of the other layer.
- BA stacking regions are regions where S atoms of layer 1 lie above an S atom of layer 2, and Mo atoms each layer do not lie above an atom of the other layer.

In Fig. S2, AB stacking regions are located at the corners of the moiré cell. AA' and BA stacking regions are located at 1/3 and 2/3 of its long diagonal, respectively.

## II. DFT TB-MOS<sub>2</sub> BANDS

Density functional theory (DFT) [54, 55] calculations based on first-principle calculations were carried out with the ABINIT code [56–58], using the local density approximation (LDA) exchange-correlation functional [60] and the Perdew-Burke-Ernzerhof (PBE) parametrized generalized gradient approximation (GGA) exchange-correlation functional [61]. We considered fourteen valence electrons of Mo ( $4s^2, 4p^6, 4d^5, 5s^1$ ), six valence electrons of S ( $3s^2, 3p^4$ ) in the

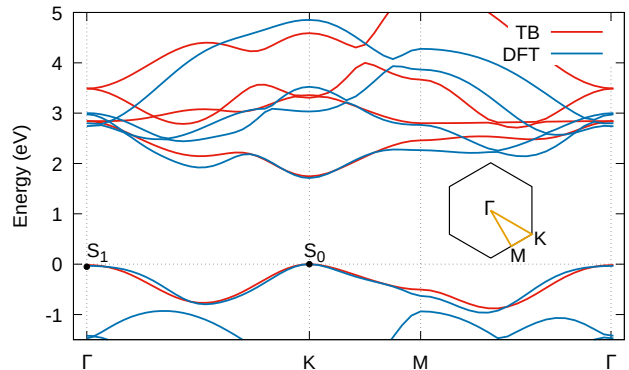


FIG. S3. DFT and TB bands in monolayer MoS<sub>2</sub>. The origin of the energy is chosen at the maximum energy of the valence band, *i.e.*, at the energy of the states labeled S<sub>0</sub>,  $E(S_0) = 0$ . Since  $E(S_1) < E(S_0)$  the gap is direct at K. The first Brillouin zone is sketched in the insert.

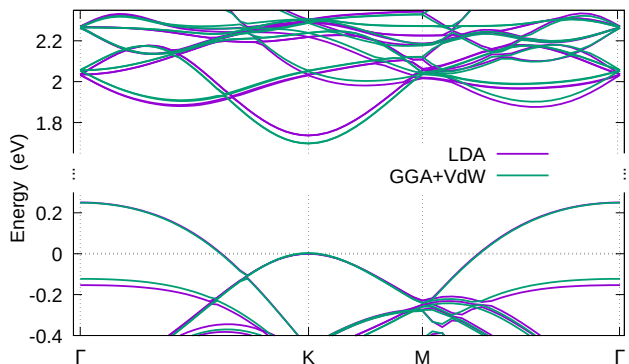


FIG. S4. DFT bands around the gap in (1,2)  $\theta = 21.79^\circ$  tb-MoS<sub>2</sub> (built from AA stacking, see Sec. IA): Comparison between LDA and the PBE-GGA + Van der Waals exchange-correlation functional.

PAW-PBE pseudopotential. The Brillouin zone was sampled by a k-point mesh of  $0.8 \text{ nm}^{-1}$  separation in reciprocal space within the Monkhorst-Pack scheme [59], and the kinetic energy cutoff was chosen to be 544.22 eV. A vacuum region of 2 nm was inserted between the MoS<sub>2</sub> bilayers to avoid spurious interactions between periodic images.

Figure S3 shows our DFT results for the band structure of monolayer MoS<sub>2</sub>. The highest energy of the valence band (state S<sub>0</sub> at the point K) is fixed to zero,  $E(S_0) = 0$ . Since the highest valence energy at the point  $\Gamma$  (state S<sub>1</sub>) has a lower energy, the gap is direct, as expected [51].

Figure S4 shows that LDA and GGA + Van der Waals approximations yield very similar results, so all further results are based on LDA calculations.

In Fig. S5, we compare the bands around the gap of (1,2) and (2,3) tb-MoS<sub>2</sub> with the monolayer case. For the purpose of comparison, the monolayer unit cell has been mapped to the bilayer one.

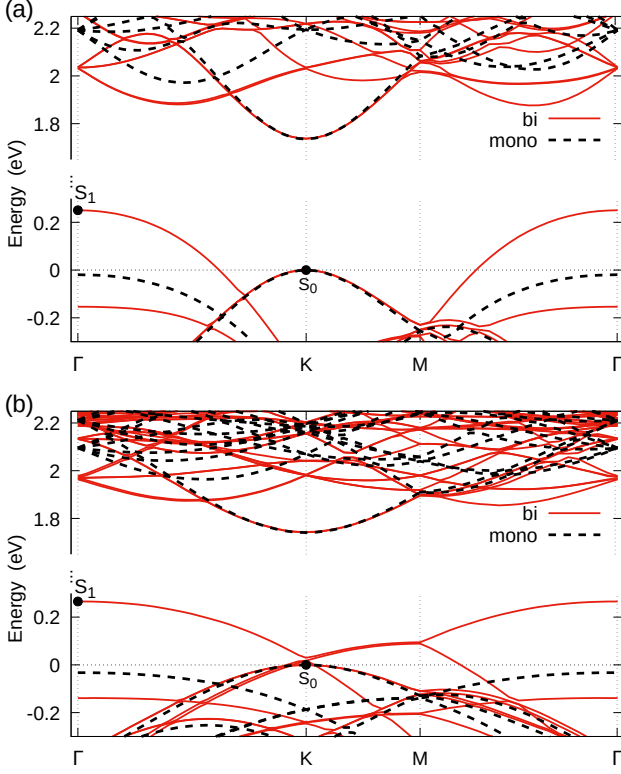


FIG. S5. DFT bands around the gap in tb-MoS<sub>2</sub> (built from AA stacking, see Sec. IA): (a) (1,2)  $\theta = 21.79^\circ$ , (b) (2,3)  $\theta = 13.17^\circ$ . (red color) bilayer, (black color) monolayer represented in the bilayer unit cell.

### III. TIGHT-BINDING (TB) MODEL

In this section, we present details of our Tight-Binding (TB) Hamiltonian for monolayer MoS<sub>2</sub> and twisted bilayer MoS<sub>2</sub>. We use a Slater-Koster scheme [42] in order to describe all the studied structures by a single set of parameters.

#### A. TB model for monolayer MoS<sub>2</sub>

We start by describing a single layer of 2H-MoS<sub>2</sub>. The lattice vectors of monolayer MoS<sub>2</sub> are  $\vec{a}_1$  ( $a\sqrt{3}/2, -a/2, 0$ ) and  $\vec{a}_2$  ( $a\sqrt{3}/2, a/2, 0$ ), with the lattice parameter  $a = 0.318$  nm. A unit cell contains 3 atoms: Mo at  $(0, 0, 0)$ , S at  $(0, a/\sqrt{3}, 0.49115a)$  and S at  $(0, a/\sqrt{3}, -0.49115a)$  [46, 51].

Our TB model includes 11 orbitals per unit cell of the monolayer: 5  $d$  Mo orbitals ( $d_0 = 4d_{z^2}$ ,  $d_1 = 4d_{xz}, 4d_{yz}$ ,  $d_2 = 4d_{x^2-y^2}, 4d_{xy}$  of 1 Mo atom) and 6  $p$  S orbitals ( $3p_x, 3p_y$  and  $3p_z$  of 2 S atoms). By symmetry, the 2  $d_1$  ( $d_2$ ) orbitals of each Mo are equivalent as well as the  $3p_x$  and  $3p_y$  of each S.

Our TB model for monolayer MoS<sub>2</sub> is an adaptation of the model proposed in Ref. [46] to our DFT results (Fig. S3). The  $pS - pS$ ,  $dMo - dMo$  and  $dMo - pS$  hopping terms are calculated using a Slater-Koster formula with the parameters  $V_{pp\sigma}$ ,  $V_{pp\pi}$ ,  $V_{dd\sigma}$ ,  $V_{dd\pi}$ ,  $V_{dd\delta}$ ,  $V_{dp\sigma}$ ,  $V_{dp\pi}$ . For the monolayer,

TABLE S2. Tight-binding (TB) Slater-Koster parameters for monolayer MoS<sub>2</sub>, and pairs of neighbors for which the hopping term is nonzero. The lattice parameter of monolayer MoS<sub>2</sub> is  $a = 0.318$  nm.

Atom	Orbitals	On-site energy (eV)
Mo	$d_0 = 4d_{z^2}$	$E_0^0 = 0.1356$
	$d_1 = 4d_{xz}, 4d_{yz}$	$E_1^0 = -0.4204$
	$d_2 = 4d_{x^2-y^2}, 4d_{xy}$	$E_2^0 = 0.0149$
S	$3p_x, 3p_y$	$E_{x,y}^0 = -38.71$
	$3p_z$	$E_z^0 = -29.45$

Atom	Neighbor	Number	Inter-atomic distance (nm)	Slater-Koster parameters (eV)
Mo	Mo	3	0.318	$V_{dd\sigma} = -0.9035$
				$V_{dd\pi} = 0.7027$
				$V_{dd\delta} = 0.0897$
S	S	6	0.241	$V_{dp\sigma} = -7.193$
				$V_{dp\pi} = 3.267$
				$V_{pp\sigma} = 8.079$
S	S	1	0.312	$V_{pp\pi} = -2.678$
				$V_{pp\sigma} = 7.336$
				$V_{pp\pi} = -2.432$
S	S	6	0.318	$V_{pp\sigma} = 7.336$
				$V_{pp\pi} = -2.432$
				$V_{pp\pi} = -2.432$

TABLE S3. TB Slater-Koster parameters for interlayer hopping terms in tb-MoS<sub>2</sub>.  $d^0$  is the interlayer distance; for the definition of  $d_{Mo-Mo}$ ,  $d_{Mo-S}$ , and  $d_{S-S}$ , see Fig. 1.

Atom	Neighbor	$d^0$ (nm)	$q$	Slater-Koster parameters (eV)
Mo	Mo	0.6800	11.6496	$V_{dd\sigma}^0 = -0.1416$
				$V_{dd\pi}^0 = -0.4254$
				$V_{dd\delta}^0 = -0.1237$
S	S	0.5238	8.9738	$V_{dp\sigma}^0 = -1.4793$
				$V_{dp\pi}^0 = 0.52431$
				$V_{pp\sigma}^0 = 6.2782$
S	S	0.3676	6.2981	$V_{pp\pi}^0 = -8.9733$
				$V_{pp\pi}^0 = -8.9733$
				$V_{pp\pi}^0 = -8.9733$

only first neighbor S-S, Mo-Mo and S-Mo hopping terms are taken into account. On-site energy values, number of neighbors taken into account, and values of Slater-Koster parameters are listed table S2.

#### B. TB model of twisted bilayer MoS<sub>2</sub> (tb-MoS<sub>2</sub>)

Now we move to tb-MoS<sub>2</sub> where we take the monolayer MoS<sub>2</sub> hopping terms of table S2 as the intralayer hopping terms. Most previous studies [23, 24, 43, 45] include only  $pS - pS$  interlayer hopping terms. At first sight, this may appear justified since these correspond to the shortest interlayer distance, see Fig. 1. However,  $d_{Mo-Mo}$  and in particular  $d_{Mo-S}$  are not that much bigger than  $d_{S-S}$  such that a sharp cutoff at the shortest distance may not be appropriate.

Indeed,  $d\text{Mo} - p\text{S}$  terms and  $d\text{Mo} - d\text{Mo}$  terms may also be important because we do not limit the interlayer coupling to first-neighbor hopping. Therefore, we include  $p\text{S} - p\text{S}$ ,  $d\text{Mo} - p\text{S}$ , and  $d\text{Mo} - d\text{Mo}$  interlayer hopping terms in our Slater-Koster scheme. Following other studies of twisted bilayer TMDCs [24] and twisted bilayer graphene [5, 48], each interlayer Slater-Koster parameter  $V_i$  is assumed to decrease exponentially as a function of the distance  $d$  between orbitals:

$$V_i(d) = V_i^0 \exp\left(-q_i \frac{d-d_0}{d_0}\right) F_c(d), \quad (2)$$

where the  $V_i^0$  is S-S  $V_{pp\sigma}^0$ , S-S  $V_{pp\pi}^0$ , Mo-Mo  $V_{dd\sigma}^0$ , Mo-Mo  $V_{dd\pi}^0$ , Mo-Mo  $V_{dd\delta}^0$ , Mo-S  $V_{dp\sigma}^0$ , Mo-S  $V_{dp\pi}^0$ , respectively;  $d_i^0$  is the corresponding interlayer distance  $d_{\text{S-S}}$ ,  $d_{\text{Mo-Mo}}$ , and  $d_{\text{Mo-S}}$ , respectively (see Fig. 1). The coefficients  $q_i$  are fixed, like in twisted bilayer graphene [48], to have a reduction by a factor 10 between first neighbor hopping and second neighbor hopping terms,

$$q_i = \frac{\sqrt{3} \ln(10) d_i^0}{(\sqrt{3}-1)a}. \quad (3)$$

Numerical values of  $V_i^0$ ,  $d_i^0$  and  $q_i$  are listed table S3.

In equation (2) a smooth cutoff function [62] is used,

$$F_c(d) = \left(1 + \exp\left(\frac{d-r_c}{l_c}\right)\right)^{-1}, \quad (4)$$

with  $r_c$  the cutoff distance and  $l_c = 0.0265$  nm [62]. For  $r \ll r_c$ ,  $F_c(r) \simeq 1$ ; and for  $r \gg r_c$ ,  $F_c(r) \simeq 0$ . All results presented in the present Rapid Communication are calculated with  $r_c = 2.5a = 0.795$  nm.

## IV. TB ELECTRONIC STRUCTURE OF TB-MOS<sub>2</sub>

### A. Analysis of the bands in tb-MoS<sub>2</sub> built from AB stacking

In the main text we showed only results for tb-MoS<sub>2</sub> built from AA stacking (see section IA). However, other types of moiré patterns exist in this system as well; in particular, one can start from AB stacking (see section IB). Figure S6 presents a comparison of the  $\theta$ -dependence of the band structure between tb-MoS<sub>2</sub> between bilayers built from AA stacking and from AB stacking. The results are qualitatively very similar, which shows that the main results of our study do not depend on the type of moiré pattern. The main quantitative differences with respect to the results discussed in the main text are the values of  $\theta_C$  and  $\theta_0$ :  $\theta_C \approx 6^\circ$  versus  $\theta_C \approx 4.5^\circ$  for tb-MoS<sub>2</sub> built from AA and AB stacking, respectively;  $\theta_0 \approx 2^\circ$  versus  $\theta_0 \approx 1.8^\circ$  for tb-MoS<sub>2</sub> built from AA and AB stacking, respectively.

### B. Local density of states (LDOS)

The TB density of states (DOS) is calculated employing a Gaussian broadening with a standard deviation  $\sigma = 2$  meV.

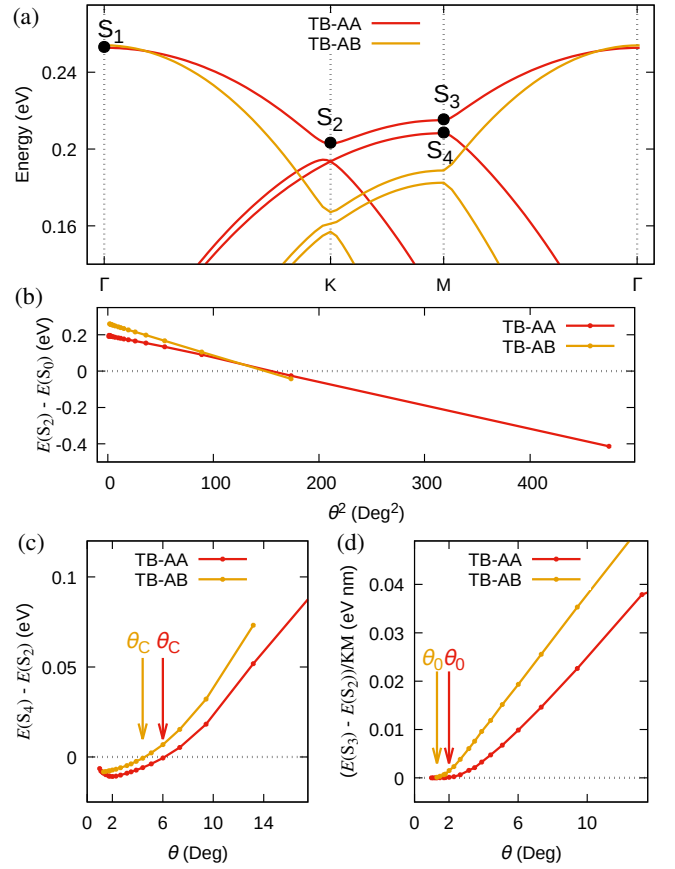


FIG. S6. Dependence of valence bands on rotation angle  $\theta$ : Comparison between tb-MoS<sub>2</sub> built from AA stacking (TB-AA, see section IA) and tb-MoS<sub>2</sub> built from AB stacking (TB-AB, see section IB). The TB-AA curves coincide with those of Fig. 4. (a) valence-band dispersion of (4,5) tb-MoS<sub>2</sub>,  $\theta = 7.34^\circ$ . (b) Energy  $E(S_2)$  of state S<sub>2</sub> (see panel (a)) versus  $\theta^2$ . (c) Energy difference between states S<sub>4</sub> and S<sub>2</sub>,  $\Delta E_{24} = E(S_4) - E(S_2)$ , versus  $\theta$ . A negative  $\Delta E_{24}$  value means that a gap  $|\Delta E_{24}|$  exists between the band below the gap and the other valence bands. (d) Average slope of  $E(\vec{k})$  of the band between states S<sub>2</sub> and S<sub>3</sub>. For every rotation angle, the origin of energy is fixed at the energy  $E(S_0)$  of the state S<sub>0</sub> (see Figs. 2 and S5).

For the  $k$ -integration we use a grid with  $Nk_x \times Nk_y$  points in the reciprocal unit cell, with  $Nk_x = Nk_y$  large enough to obtain a DOS that is independent of these parameters. Due to this broadening, the minigaps found in the band structure are not always seen clearly in the DOS.

Figure S7 shows the LDOS for the  $d_0 = d_{z^2}$  orbital of an Mo atom at the center of the AA stacking region for several rotation angles  $\theta$ . Figure S8 (top panel) shows the local density of states (LDOS) of the  $d_0 = d_{z^2}$  Mo orbital for the selected rotation angle  $\theta = 5.09^\circ$ , but for Mo atoms located at different stacking regions of the moiré pattern (see section I). Confined states (“flat bands”) lead to sharp peaks in the LDOS (Fig. S7). These states have  $d_{z^2}$  Mo character (Fig. S8 (bottom panel)), and a very small weight for the other  $d$  Mo orbitals. The flat bands are mainly located in the AA stacking region (Figs. S8 (top panel) and S9). Figure S9 shows that the lowest-energy

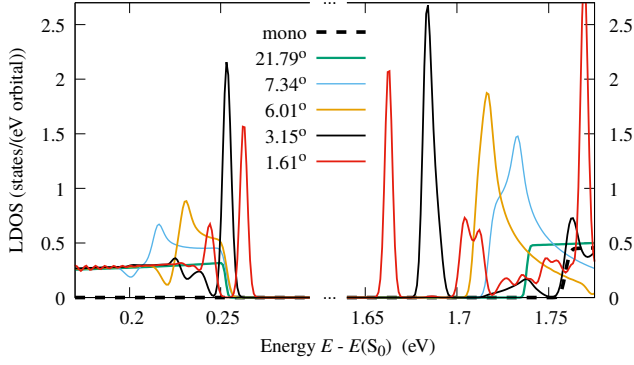


FIG. S7. TB local density of states (LDOS) of the  $4d_{z^2}$  Mo orbital at the center of the AA stacking region for different rotation angles of tb-MoS<sub>2</sub>. The LDOS is calculated employing a Gaussian broadening with a standard deviation  $\sigma = 2$  meV.

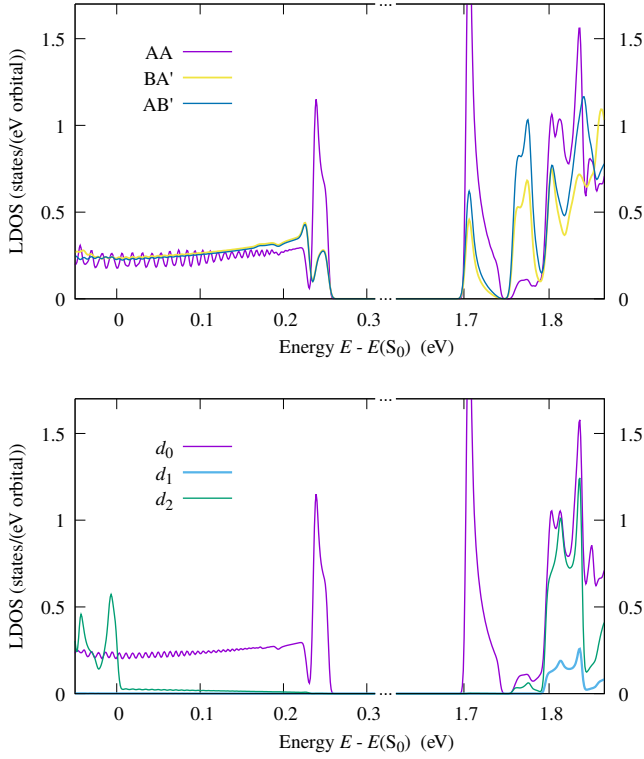


FIG. S8. TB local density of states (LDOS) of the Mo orbital around the main gap in (6,7)  $\theta = 5.09^\circ$  tb-MoS<sub>2</sub> (built from AA stacking, see Sec. IA): (Top panel) LDOS of the  $d_0 = d_{z^2}$  Mo orbital at the center of AA, BA', and AB' stacking regions (Sec. IA). (Bottom panel) LDOS of  $d_0$ ,  $d_1 = 4d_{xz}$ ,  $4d_{yz}$  and  $d_2 = 4d_{x^2-y^2}$ ,  $4d_{xy}$  Mo orbitals at the center of the AA stacking region. The LDOS is calculated employing a Gaussian broadening with the standard deviation  $\sigma = 2$  meV.

flat bands in the conduction and valence bands correspond to Mo atoms that are located at the center of the AA stacking

regions, and that the next flat band in the conduction and valence bands corresponds to states located in a ring in the AA stacking regions.

### C. Eigenstates corresponding to flat bands in tb-MoS<sub>2</sub>

Analysis of the band dispersion (Fig. 5) shows that the first isolated flat band below the main gap (valence band) is non-degenerate and thus contains one state per moiré cell. By contrast, the two first isolated flat bands above the gap (conduction bands) are two-fold quasi degenerate. The weight of the eigenstates corresponding to these flat bands is mainly concentrated on  $d_0 = d_{z^2}$  Mo orbitals (more than 98% and 95%, respectively) located at the center of AA stacking regions. This is shown in Fig. S9(b,c) for eigenstates at the points  $\Gamma$ , K, and M of the flat band above and below the main gap, respectively.

For small enough angles, the next isolated flat bands (Fig. 5(b)) are four-fold quasi degenerate in the conduction band and two-fold quasi degenerate in the valence band. The weight of the eigenstates, corresponding to these flat bands at the points  $\Gamma$ , K, and M, is mainly located in a ring in AA stacking regions (Fig. S9(a,d)).

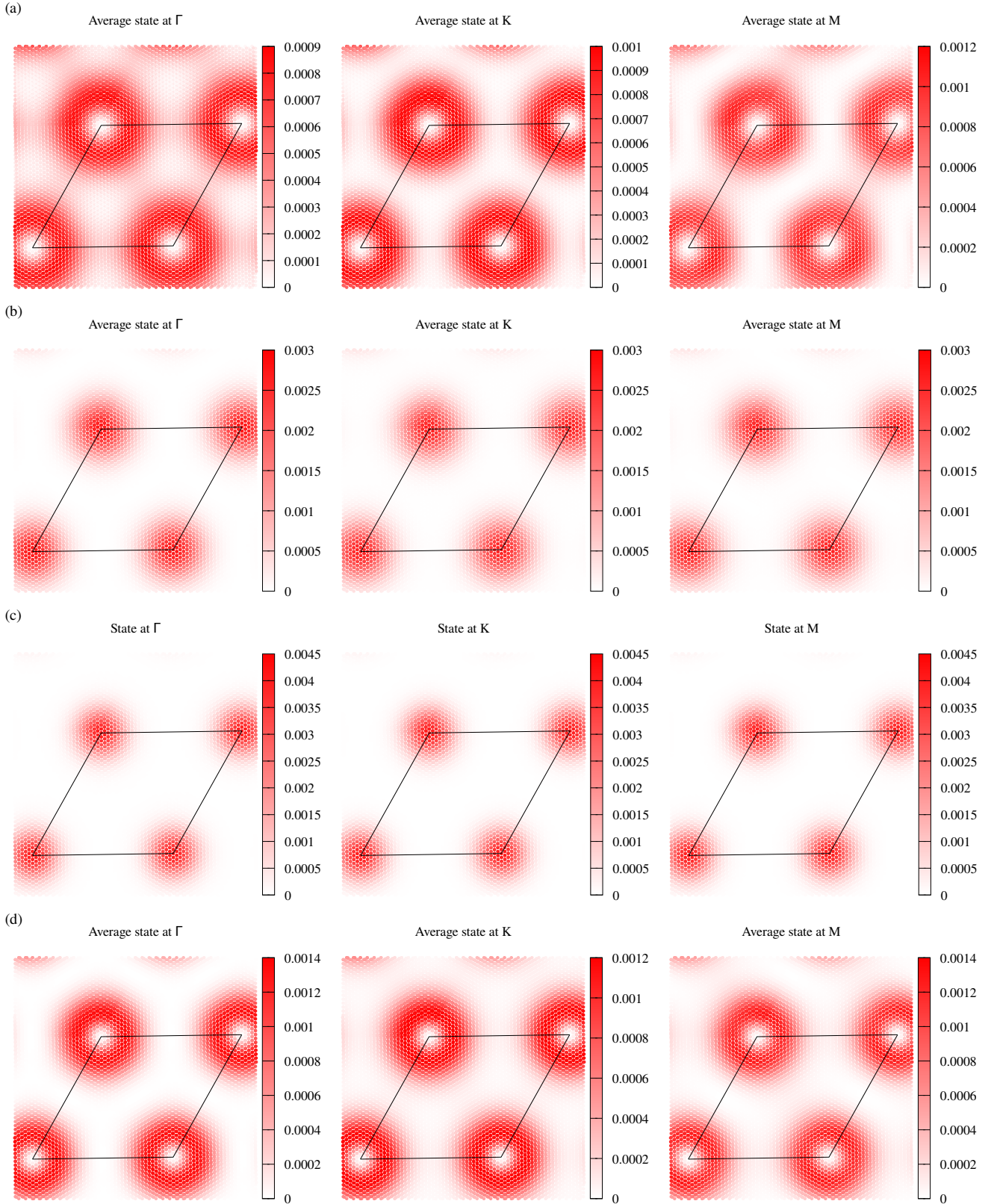


FIG. S9. Average weight of the eigenstates at  $\Gamma$ , K, and M, of the flat band around the gap in real space in (20, 21) tb-MoS<sub>2</sub> (built from AA stacking, see Sec. IA) with a rotation angle  $\theta = 1.61^\circ$ : Conduction band: (a) Average of the four-fold quasi-degenerate band at energy  $E \simeq E(S_0) + 1.686 \pm 0.002$  eV and (b) average of the two-fold quasi-degenerate band at energy  $E \simeq E(S_0) + 1.6626 \pm 0.0002$  eV. Valance band: (c) non-degenerate bands at energy  $E \simeq E(S_0) + 0.26249 \pm 0.00001$  eV, and (d) average of the two-fold quasi-degenerate band at energy  $E \simeq E(S_0) + 0.2518 \pm 0.0003$  eV. The corresponding bands are shown in Fig. 5(b). The color scale shows the weight of the eigenstate on each  $d_0 = 4d_z$  orbital of the Mo atoms. The sum of these weights is more than 98% and 95% of each state for the valence and conduction band, respectively. Black lines show the unit cell containing 2522 Mo atoms. AA stacking regions are at the corners of this cell.